MICRO ELECTRO MECHANICAL SYSTEMS INTEGRATED FREQUENCY RECONFIGURABLE ANTENNAS FOR PUBLIC SAFETY APPLICATIONS

by

Hema Swaroop Mopidevi

A thesis submitted in partial fulfillment
of the requirements for the degree

of

MASTER OF SCIENCE

in

Electrical Engineering

Approved:

Dr. Bedri A. Cetiner Major Professor	Dr. Jacob Gunther Committee Member
Dr. Edmund A. Spencer Committee Member	Dr. Byron R. Burnham Dean of Graduate Studies

UTAH STATE UNIVERSITY
Logan, Utah

2010

Abstract

Micro Electro Mechanical Systems Integrated Frequency Reconfigurable Antennas for Public Safety Applications

by

Hema Swaroop Mopidevi, Master of Science

Utah State University, 2010

Major Professor: Dr. Bedri A. Cetiner
Department: Electrical and Computer Engineering

This thesis work builds on the concept of reconfiguring the antenna properties (frequency, polarization, radiation pattern) using Radio Frequency (RF) Micro Electro Mechanical Systems (MEMS). This is a part of the overall research performed at the RF Micro/Nano Electro Mechanical Systems (μNϵMS) Laboratory at Utah State University, which includes design, microfabrication, test, and characterization of μNϵMS integrated cognitive wireless communication systems (Appendix A).

In the first step, a compact and broadband Planar Inverted F Antenna (PIFA) is designed with a goal to accommodate reconfigurability at a later stage. Then, a Frequency Reconfigurable Antenna (FRA) is designed using MEMS switches to switch between the Public Safety (PS) bands, 152-162 MHz and 406-512 MHz, while maintaining the integrity of radiation pattern for each band. Finally, robust mechanical designs of the RF MEMS switches accompanied by different analyses have been performed. These analyses are instrumental in obtaining high yield, reliable, robust microfabrication processes including thin film metal deposition and patterning.

(51 pages)

To my beloved family and friends.

Acknowledgments

I would like to express my highest regards and gratitude to my advisor and mentor, Dr. Bedri A. Cetiner, who believed in me right from the beginning of my career as a research assistant at USU. He not only gave me the required knowledge to pursue my research through the subjects he taught, but also always gave the required moral support during my hard times. He inculcated in me a never-ending motivation and zeal towards my research efforts, as well as encouraged my presentation skills on a regular basis. I would like to express my gratitude to Dr. Mehmet Unlu, who gave me a thorough experience to work on CoventorWare and MEMS design through his vast practical knowledge. I would like to thank my committee members, Dr. Edmund A. Spencer and Dr. Jacob Gunther, who extended their support.

I would like to thank all my friends in Logan: Chandu, Kalyan, Pradeep, Nagi, Atul, Meena, Jahnavi, Amrita, and the list goes on. I never felt lonely or dejected, and the only reason I never missed my parents is the unending support they have given. I would also like to thank my friends at RF MEMS lab: Ali; Dani, who was our visiting scholar from Spain; Yuan; and Yasin for their help on various occasions. I would like to especially thank Dani for sharing his expertise on antenna design and Ali for his generous help in drawing some figures. I would also like to emphasize the importance of our joint efforts in the design phase of the antenna. I realize how important it is to work as a team on research projects.

Lastly, the constant love and affection from my parents is the backbone of any successful endeavor in my life. Without their constant support and encouragement for quality education I would never have achieved the right kind of exposure to fulfill my dream of working in my area of interest.

Hema Swaroop Mopidevi

Contents

List of Tables

List of Figures

Acronyms

BW	Bandwidth
FEM	Finite Element Method
FRA	Frequency Reconfigurable Antenna
HFSS	High Frequency Structure Simulator
MEMS	Micro Electro Mechanical Systems
MIMO	Multiple Input Multiple Output
MPD	Material Properties Database
MRA	Multi-Functional Reconfigurable Antenna
PIFA	Planar Inverted F Antenna
PS	Public Safety
RF	Radio Frequency
SER	Symbol Error Rate
US	United States

Chapter 1

Introduction

This age of rapid technological development demands an ever-increasing speed of information transfer over the wireless communication systems for the sake of ease and speed of access of useful information. The existing wireless communication systems need a massive update both in the communication aspect and Radio Frequency (RF) perspective because with today's advent of smart phones, i-touch, i-pad, etc., the demand on efficient use of Bandwidth (BW) in the wireless communication scenario has increased many a times. Several coding and multiplexing schemes [1] have evolved in the signal processing domain for this purpose but these require multiple antennas at the RF end for better performance. Multiple Input Multiple Output (MIMO) systems [2–7] make the best use of such intelligent coding schemes provided they can be benefitted from the adaptability in the antenna design - a single antenna capable of performing multiple functions of several antennas by dynamically changing its geometrical properties, i.e., Multi-functional Reconfigurable Antenna (MRA).

The dynamic changes encountered in the propagation medium, the ever-increasing demand of wireless services such as voice, video, multi-media, internet on phone, etc., the need of dynamic behavior of the antenna to suit to the above scenario have resulted in the idea of MRA [8–13]. In an adaptive MIMO system, capable of increasing the capacity of the next-generation wireless communication systems, emphasis has been made on smart coding techniques in the signal processing domain making use of dumb antenna arrays with fixed properties like radiation, polarization, operation frequency, etc. Therefore, introducing adaptability in the antenna design allows an additional degree of freedom in an adaptive MIMO system selecting the best antenna performance in accordance to the transmission algorithm and varying channel conditions. This explains the significance of MRA which can

dynamically change their functionality like frequency of operation, beam-tilt, polarization, etc., by mere operation of Micro Electro Mechanical Systems (MEMS) switches [14–17]. In effect, the principle of reconfigurable antennas: adaptable change of the geometry of the antenna by operation of MEMS switches resulting in multiple functionality is extremely useful in MIMO scenario for efficient use of BW. The invention of microwave laminate compatible RF MEMS technology [18,19] by Dr. Bedri A. Cetiner has eased and expedited the fabrication process of MRAs. MEMS switches are the main building blocks of MRAs, and hence robust and harsh environment tolerant MRA design requires maximizing the reliability of MEMS switches providing an acceptable RF performance over a wide frequency range (Appendix A).

Recent developments in the MIMO systems resulting in the improvement of indoor channel (IEEE-802.11n model F and B) link performance is mainly possible by the use of MRAs in the RF chains [20]. Each MRA replaces the functionality of significant number of antennas thereby reducing the number of RF chains when compared to the legacy multi antenna systems. As a result, the capacity of the wireless communication MIMO system equipped with arrays of MRAs is maximized with a corresponding decrease in the Symbol Error Rate (SER), hence outperforming the systems with conventional antennas. The gain of a typical adaptive MIMO system equipped with reconfigurable antennas is also quite high when compared to the dumb antenna arrays with properties fixed at the beginning of the design.

Latest developments in the information theory resulting in a new multiplexing scheme in MIMO systems called interference alignment [21–24] have led to the ever-increasing demand of reconfigurable antennas. Induced channel fluctuations by predetermined switching patterns resulting in different modes of multiple antennas lead to the distribution of half of the total channel capacity to N users [25–28]. Instead of using multiple antennas in this scenario, use of an array of MRAs increases the intelligence of the RF end where in the reconfigurable antennas and the intelligent coding schemes of the signal processing domain work hand in hand in an effective feed-back loop. In this aggressive approach of intelligent

use of channel capacity the speed of switching of the reconfigurable antenna is an important design problem which relates directly to the switching speed of MEMS.

In this thesis, the frequency reconfigurability of an MRA has been explored with a goal to switch between the United States (US) Public Safety (PS) bands 152 - 162 MHz and 406 - 512 MHz. The flow of this research is divided into three important steps. First, a broadband antenna which can support interoperability with a compact structure is designed in order to provide a basic antenna structure for reconfigurability. In the second step, a robust frequency reconfigurable antenna with minimal number of switches is designed which also maintains the integrity of radiation pattern at different frequencies. Last, a robust mechanical design of RF MEMS switch which forms the fundamental building block of the MRA is explained which is essential for the success of this design.

Chapter 2

Broadband and Compact PIFA

2.1 Introduction

During natural or man-made catastrophes, there is a need for a robust wireless communication system with broad BW to support wireless communication needs (voice, data, and video) of the US PS community. The broad bandwidth is also needed to accommodate the interoperable communications among a large number of emergency responders of various agencies trying to jointly handle the situation. Mobile devices require compact antennas and the Planar Inverted F Antenna (PIFA) presented here suits this purpose well. The BW of a legacy PIFA [29, 30] however, is typically less than 10%. Various BW enhancement techniques of PIFAs such as using a T-shaped ground plane [31], tapering of the patch [32], and dual resonant patches [33], have been commonly used in the literature. In this chapter we combine T-shaped ground plane and patch tapering [31, 32] techniques in conjunction with the capacitively coupled feed method [34] in a PIFA structure so as to achieve substantial BW improvement. The presented PIFA operates over 675.5 – 953 MHz, resulting in 34.7% BW for VSWR<2 with good gain flatness.

2.2 Design and Working Mechanism

The three aforementioned techniques, which are eventually combined into a single PIFA structure to achieve an optimal design with broad BW, are discussed below.

2.2.1 T-Shaped Ground

The T-shaped ground technique [31] emphasises the effect of the ground planes geometrical features on BW with the top plane patch element dimensions being fixed for a given resonant frequency. The BW of a PIFA can be enhanced by properly shaping the ground

plane; hence the ground plane is transformed to a T-shape by etching away two rectangular patch shape regions (of which boundaries are indicated by dashed lines in fig. 2.1) of copper layer from it. Ideally, the ground plane metal is placed on an air substrate. However, in this work, for the sake of mechanical integrity and ease of fabrication, the T-shaped ground plane is formed on a thin dielectric substrate ($d \sim 0.8mm$, with ϵ_r close to 1). The copper layer on one side is etched away completely, while the other side is etched into a T-shape copper. As simulations demonstrated, this simplification does not change the behaviour of

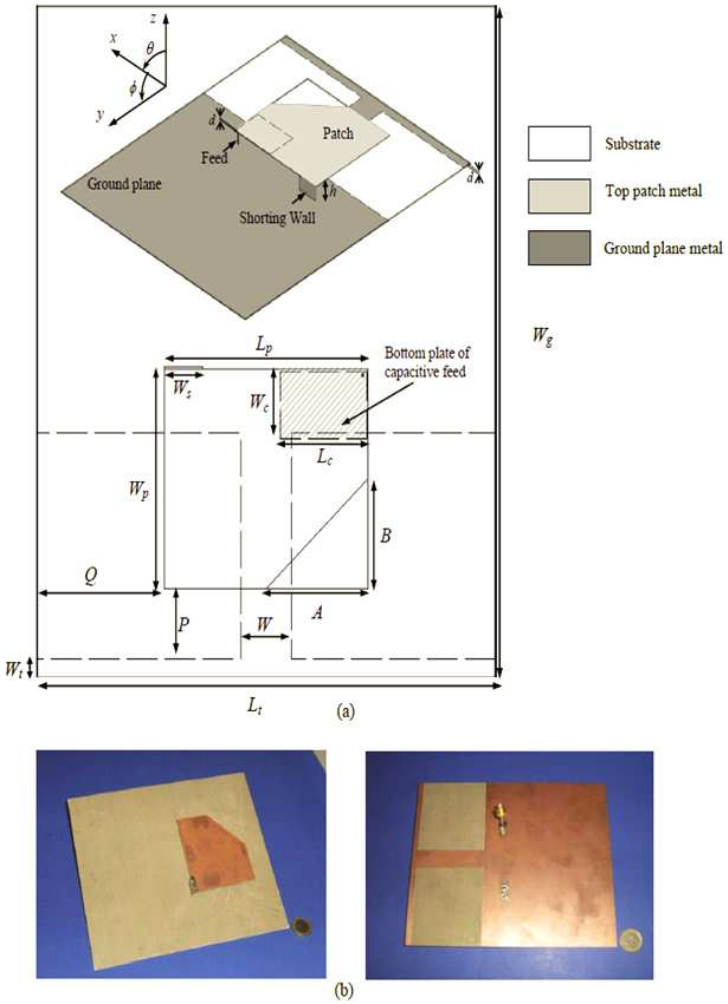

Fig. 2.1: 2D and 3D schematics of proposed PIFA and photographs of fabricated PIFA (top and bottom views) indicating metal boundaries of hidden views of PIFA (T-shape ground and bottom plate of capacitive feed) in 2D and 3D schematics: a) 2D and 3D schematics of the proposed PIFA, b) Photographs of the fabricated PIFA.

the antenna. The main design parameters for the T-shape ground plane are W, W_t, W_g, and L_t as depicted in fig. 2.1.

2.2.2 Patch Tapering

Given the limited volume available for antenna elements in wireless communication devices, this BW enhancement technique [32] employs a linear tapering of the radiation patch by simple geometrical modification of the original design, as opposed to common techniques that use additional elements or increase the volume of the antenna. The essential design parameters are length and width of the top patch, L_p, W_p, and the tapering lengths A and B as shown in fig. 2.1.

2.2.3 Capacitive Coupling

This type of feeding is used to compensate for the inductance of the coaxial feed line by means of terminating it with a capacitor patch [34]. The result is a better match in a wider frequency range. Also, the use of capacitor feeding helps in easy fabrication and there is no need to connect the coaxial feed directly to the top patch. As explained in the T-shaped ground plane sub section, instead of using air as a dielectric for the capacitive feed, a substrate ($d \sim 0.8mm$, with ϵ_r close to 1) is sandwiched by the bottom conductive plate of the capacitive feed and top patch metal of the PIFA. The design parameters of this type of feeding are L_c and W_c, the size of the bottom conductive plate, which is placed underneath the tapered radiation patch with a distance as determined by the thickness of the substrate ($d \sim 0.8mm$) as shown in fig. 2.1.

2.3 Final Design

Initially, a coaxial fed PIFA using only one of the BW enhancement techniques, i.e., the T-shaped ground plane, is designed, resulting in an impedance BW of 18%. The location of the feed is jointly optimised with the design parameters and is fixed for the rest of the design (which is located at one corner of the patch). Then, for the second technique, a patch taper is introduced into the same design without making any changes in the T-shaped ground

plane and feed mechanism. The BW of the combined design is more than 26%, but the operational frequency is increased as patch tapering is introduced. To account for this increase, the parameters of the T-shape are varied, simultaneously changing the width of the shorting wall W_s as depicted in fig. 2.1. The final step is to change the feeding from coaxial cable to a capacitively coupled feed and to obtain a good match by optimising the parameters of feeding. The BW of the final design in High Frequency Structure Simulator (HFSS) simulation is $\sim 31\%$, as shown in fig. 2.2. The direction of the maximum gain of the final design is tilted in a particular direction (in $\Phi = 90^0$ cut of the total electric field the maximum gain is in $\theta = 30^0$ direction), as shown in fig. 2.3.

2.4 Final Design Dimensions

The final dimensions of the PIFA in millimetres as derived from the previous section are shown in fig. 2.1: the patch, L_p X W_p is 80 X 72; the height of the patch, $h = 10$; the location of the patch, $Q = 50$, $P = 23$; the tapering lengths, $A = 40$, $B = 36$; the ground plane parameters L_t X W_g is 180 X 220, $W = 20$; $W_t = 6$; the capacitive feed metallisation plate, L_c X W_c is 34 X 22; the width of the shorting wall is $W_s = 15$.

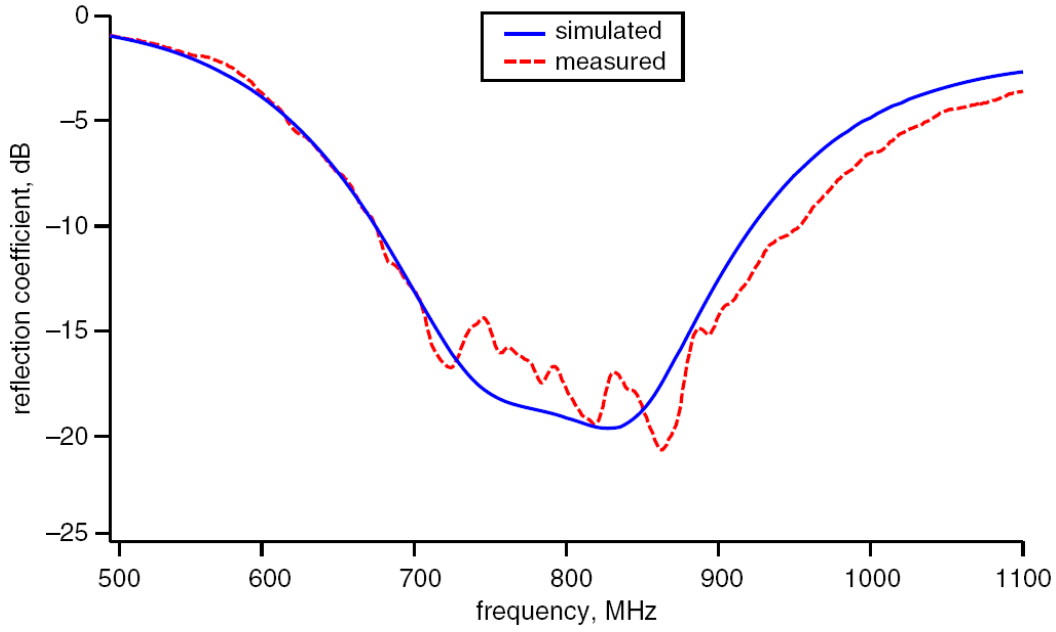

Fig. 2.2: Measured and simulated reflection coefficients of PIFA.

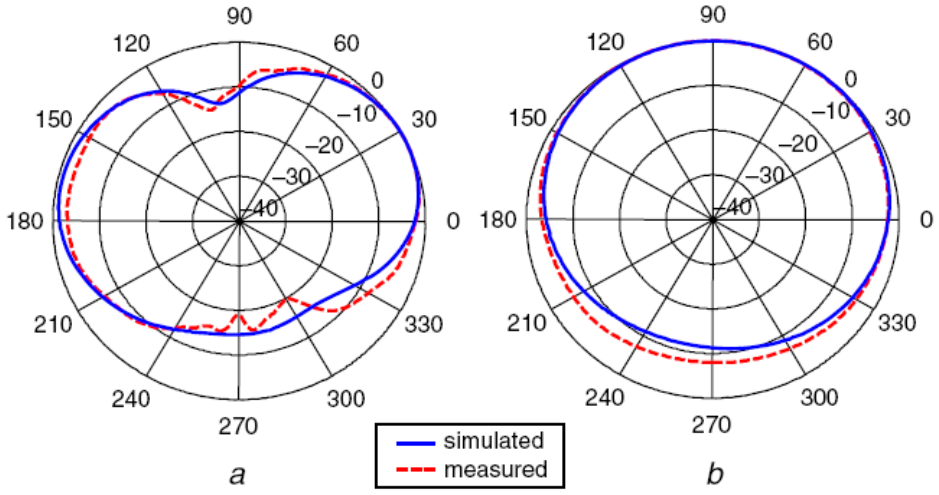

Fig. 2.3: Total normalised electric field intensity at 800 MHz for $\Phi = 90^0$ plane and $\theta = 30^0$ plane: a)$\Phi = 90^0$ plane, b)$\theta = 30^0$ plane.

2.5 Fabrication and Measurements

A PIFA with the above dimensions was fabricated and its radiation and impedance behaviour have been characterised. The fabrication involves copper layer removal by mechanical etching to define the planar geometrical features of different parts of the antenna. The bottom metal plate of the capacitive feed was etched on one side of the substrate, and the tapered patch layer is formed on the other side, which also contains the top metallisation of the feed. The T-shaped ground plane is formed on a separate substrate as explained in the Design and Working Mechanism section. Finally, these individual layers, along with the vertical wall and coaxial cable, were soldered together to obtain the 3D architecture of the PIFA. The inner conductor of the coax is attached to the bottom metallisation of the capacitive feed through the ground plane and the outer conductor directly to the ground plane. The measured reflection coefficient of the fabricated antenna results in broader BW ($\sim 35\%$) compared to the HFSS simulation with the centre frequency of 800 MHz as shown in fig. 2.2. The radiation patterns showing the normalised total electric field intensity in two planes ($\Phi = 90^0$ and $\theta = 30^0$ planes) at 800 MHz are given in fig. 2.3. $\theta = 30^0$ plane is deliberately chosen since the maximum gain direction is oriented along this direction. The radiation patterns (Appendix B) at 700 and 900 MHz are also measured and simulated,

showing almost identical patterns to those of 800 MHz. The maximum gain with respect to frequency showing a good flatness is illustrated in fig. 2.4. Measured and simulated results agree well, as is clear from these figures.

2.6 Conclusion

The presented PIFA uses a combination of two BW enhancement techniques and capacitive feeding, which provides $\sim$ 35% bandwidth. This antenna is well suited to the robust and interoperable wireless communication needs of the United States Public Safety community. The presented PIFA maintains its radiation pattern with an average gain of nearly 4.2 dB over the 675.5 – 953 MHz frequency band covering three of the Public Safety bands. Measured results agree well with simulations.

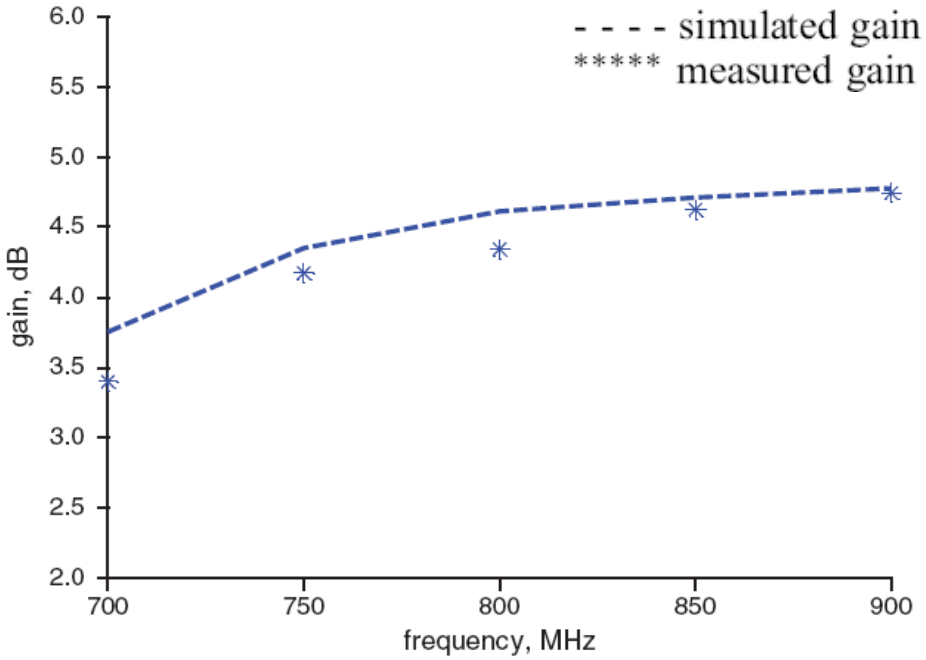

Fig. 2.4: Measured and simulated gains with respect to frequency.

Chapter 3

Frequency Reconfigurable Antenna

3.1 Antenna Architecture

Achieving a wide-bandwidth with a compact antenna while maintaining the integrity of the radiation pattern is the principal agenda we have incorporated into this successful Frequency Reconfigurable Antenna (FRA) design which can cover 152 – 162 MHz band in Mode1 and 406 – 512 MHz band in Mode2. Planar Inverted F Antenna (PIFA) [29] popularly used in mobile communications, is used individually for each mode as a first step in reducing the size of the antenna in mobile/wireless communication scenario. Two bandwidth enhancement techniques of PIFA namely T-shaped ground-plane and patch tapering are combined and optimized. A dielectric RO4003C (with $\epsilon_r = 3.38$, $\tan\delta = 0.002$) is used as a substrate to make it micro-fabrication compatible and also for the purpose of size – reduction and feeding is through coaxial cable. The capacitive feed layer mentioned in the previous design in Chapter 2 [35] is removed with a goal to avoid reconfigurability in multiple layers thereby reducing the complexity of the antenna. The meandered line introduced in the pole of the T-shaped layer of PIFA, as shown in fig. 3.1, has a considerable effect of size-reduction as the pole is the major radiating element. The specific dimensions of PIFA corresponding to both the modes (Mode1 and Mode2) in mm are in fig. 3.1 as: The patch, L_p X W_p is 106 X 108; height of the patch, $h = 25$; tapering lengths, $A = 84$, $B = 81$; ground plane parameters, L_t X W_g is 195 X 180; width of the pole $W_P = 33$; width of T-shape $W_T = 40$; width of the shorting wall, $W_s = 40$; length of the meander $L_m = 341.58mm$; is not shown in fig. 3.1 as it represents the entire length of the meandered line, width of the meandered line $W_m = 3$. The position of the individual MEMS switch for each mode and its operation is discussed elaborately in Frequency Reconfigurability section.

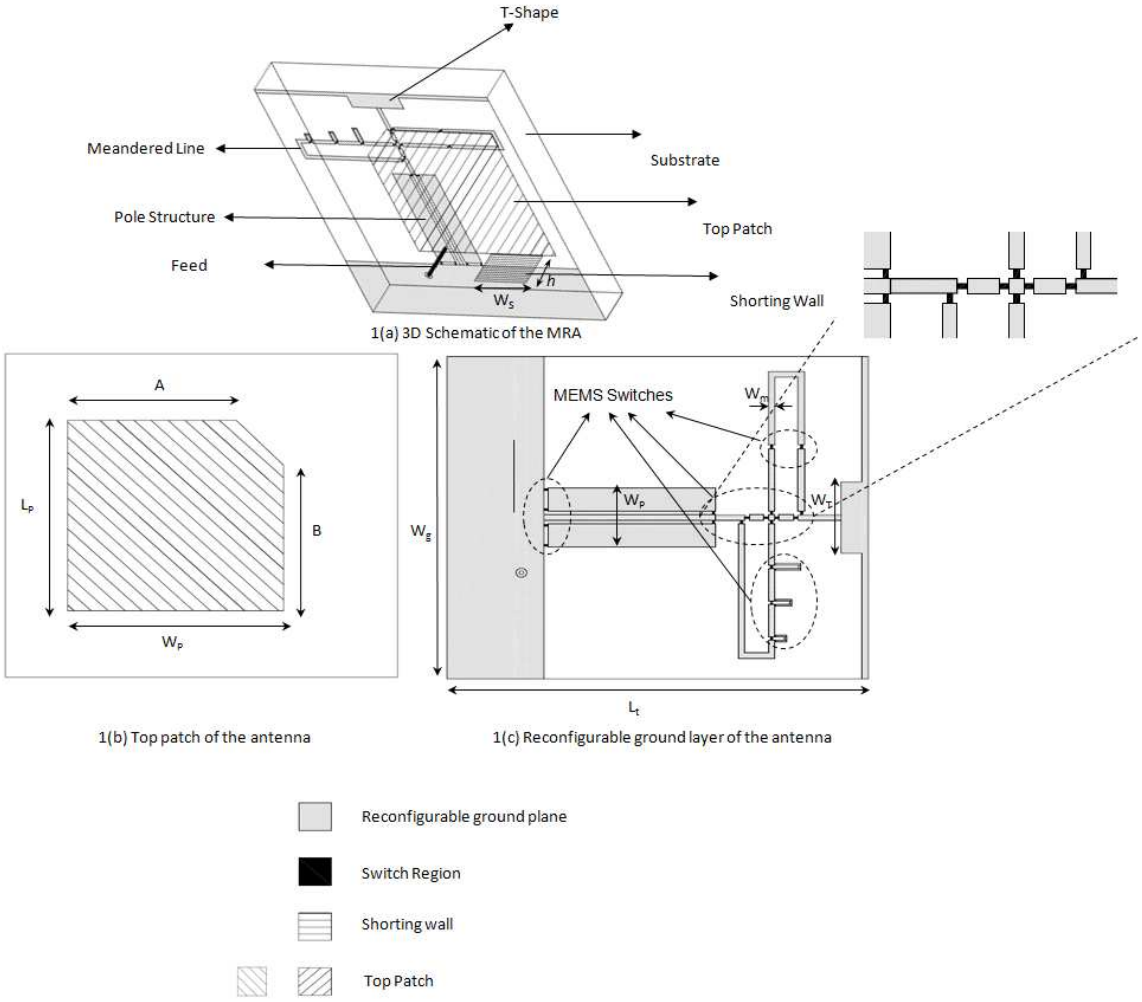

Fig. 3.1: 2D and 3D schematics of the antenna structure: a) 3D schematic of the MRA, b) Top patch of the antenna, c) Reconfigurable ground layer of the antenna.

3.2 Frequency Reconfigurability (150, 400 – 500 MHz Bands)

A robust design which can facilitate both Mode1 (152 – 162 MHz) and Mode2 (406 – 512 MHz) by operating the MEMS switches ON or OFF is given here. The success of this design lies in confining the reconfigurability to one layer i.e., the ground layer of the PIFA. In this design, the pole in the reconfigurable ground layer becomes the major radiating element and dominates the radiation pattern of the patch and its increased width results in high bandwidth. Hence, creating a meander in the pole leads to a decrease in the overall size (which is dominated by the lowest operational frequency of the designed FRA) of the antenna. Several attempts of preserving the T-shape of the structure at various locations in

the ground plane, which is an important design consideration at different frequencies, lead to the idea of connecting the pole-structure to the T-shape to make it resonate at a higher frequency. Figure 3.1(a) and fig. 3.1(b) give the 3D schematic of the antenna and the top view of the same, respectively. The MEMS switches are strategically located on the pole and meandered part of the ground plane as shown in fig. 3.1(c) to incorporate frequency reconfigurability into the antenna design. Except for the ground plane, the rest of the parameters or the dimensions of different parts of the design are the same for both modes of operation. A design trade-off between the size of the antenna, bandwidth obtained, and integrity of the radiation pattern resulted in an increase in the number of switches used in the ground layer.

3.2.1 Mode1 (152 – 162 MHz)

The overall size of the MRA is limited to 19.5 X 18 X 2.5 cm^3 which is less than $\lambda/10$ at 150 MHz. The BW of this design in Mode1 is narrow (about 0.5 MHz) as we had to compromise on the size of the antenna while maintaining an omni-directional radiation pattern in the $\phi = 0^0$ plane. The reconfigurability in the meandered line in Mode1 (which is attributed by Ali Khoshniat, master's student in Electrical Engineering, Utah State University) by the MEMS switches L_1 to L_9 are shown in fig. 3.2. The magnified sub-figure of fig. 3.2 shows how the three MEMS switches (L_1, L_4, and L_7) on the meandered line can give 23 combinations by creating a longer path for the RF signal at each MEMS switch (when it is OFF), thereby decreasing the operational frequency of the overall design. Each bypass has two more MEMS switches and these are in OFF state when the main switch (L_1, L_4, or L_7) is ON and vice versa. This is required to avoid the coupling effect of the nearby lines on the sub-meandered lines. An important point to be noted in this context is that the RF signal always takes the shortest possible path and this is why it passes through the switch when it is closed, avoiding the longer route. In this way, in spite of having a low bandwidth, we can fine tune the operational frequency in Mode1 to sweep from 152 – 162 MHz with a different combination of the ON and OFF states of the MEMS switches in the meandered line. The fine tuning capability of this design is shown in fig. 3.3 where in

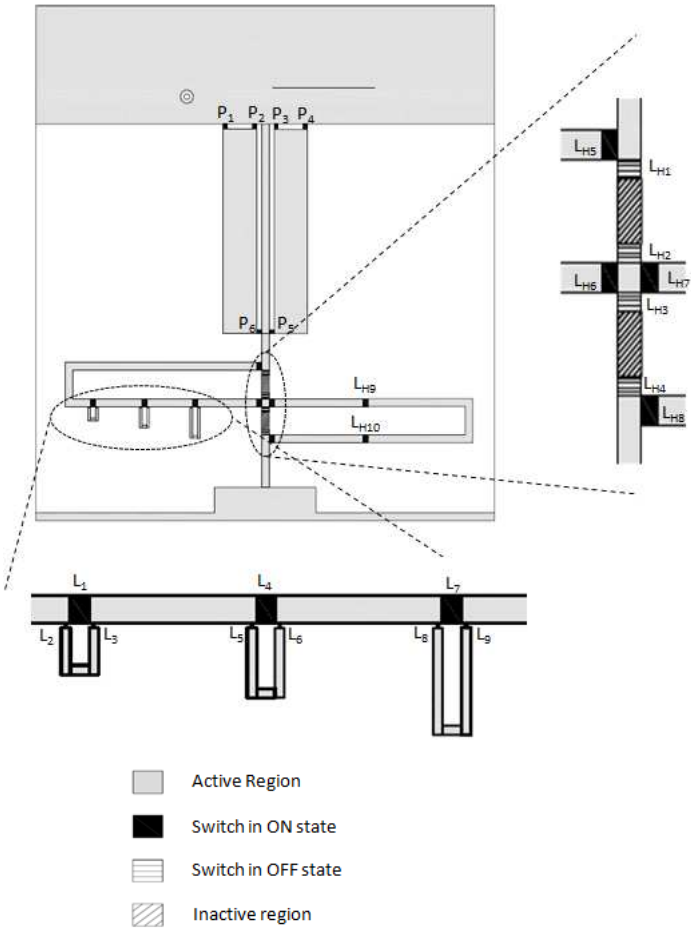

Fig. 3.2: Reconfigurable ground layer in Mode1.

the reflection coefficient of fine tuned modes are depicted. Please note that the number of switches for fine tuning and the BW obtained at a single frequency are not optimized, and at the end we may use four to five sub-meandered sections each having three MEMS switches in turn to sweep the frequency over the entire band in Mode1. The radiation pattern of Mode1 at any frequency in the band is omni-directional in the $\Phi = 0^0$ plane proving the robustness of the design. As an example, a typical radiation pattern at 157 MHz is shown in the fig. 3.4. The switches L_{H1} to L_{H10} operate in such a way that the RF signal passes through the meandered line avoiding the straight line path to the T-shape as shown in fig. 3.2. The width of the pole structure for Mode1 is 33 mm which is obtained by turning the switches P_1 to P_6 ON always.

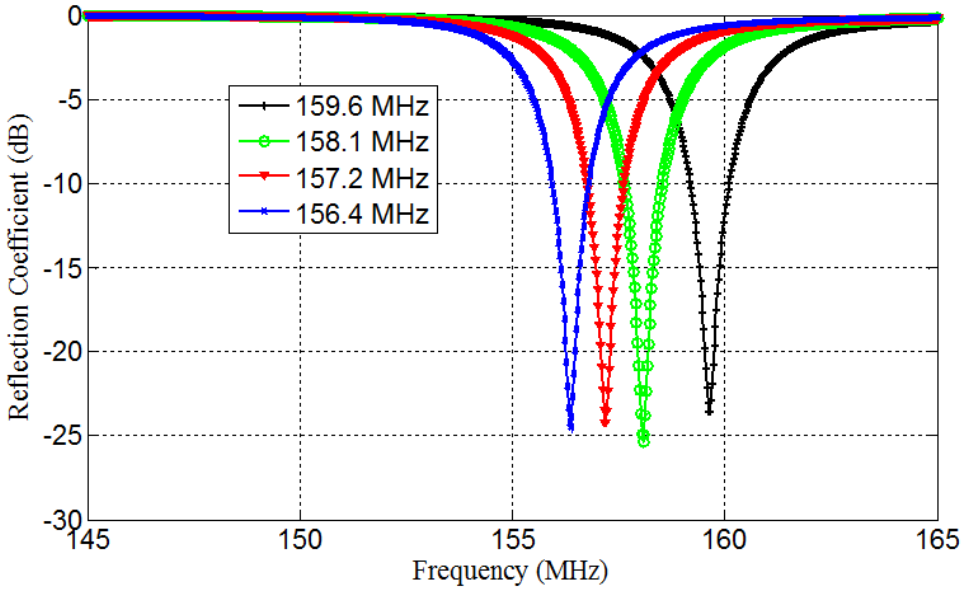

Fig. 3.3: Reflection coefficient of Mode1 depicting fine tuning capability.

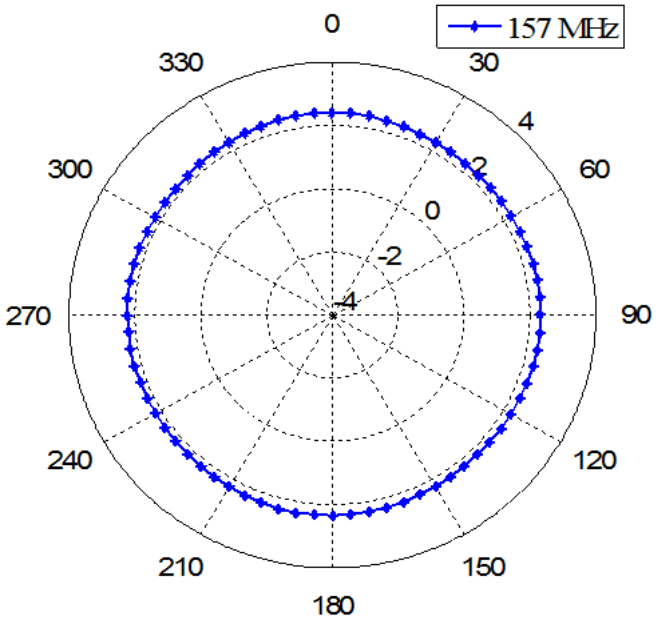

Fig. 3.4: Radiation pattern at a sample frequency in Mode1.

3.2.2 Mode2 (406 – 512 MHz)

The noticeable changes from Mode1 to Mode2 are the reconfigurability in the pole structure of PIFA and RF signal avoiding the meander path by travelling through a straight line to the T-shape as shown in fig. 3.5. The meander is avoided with a goal to make the

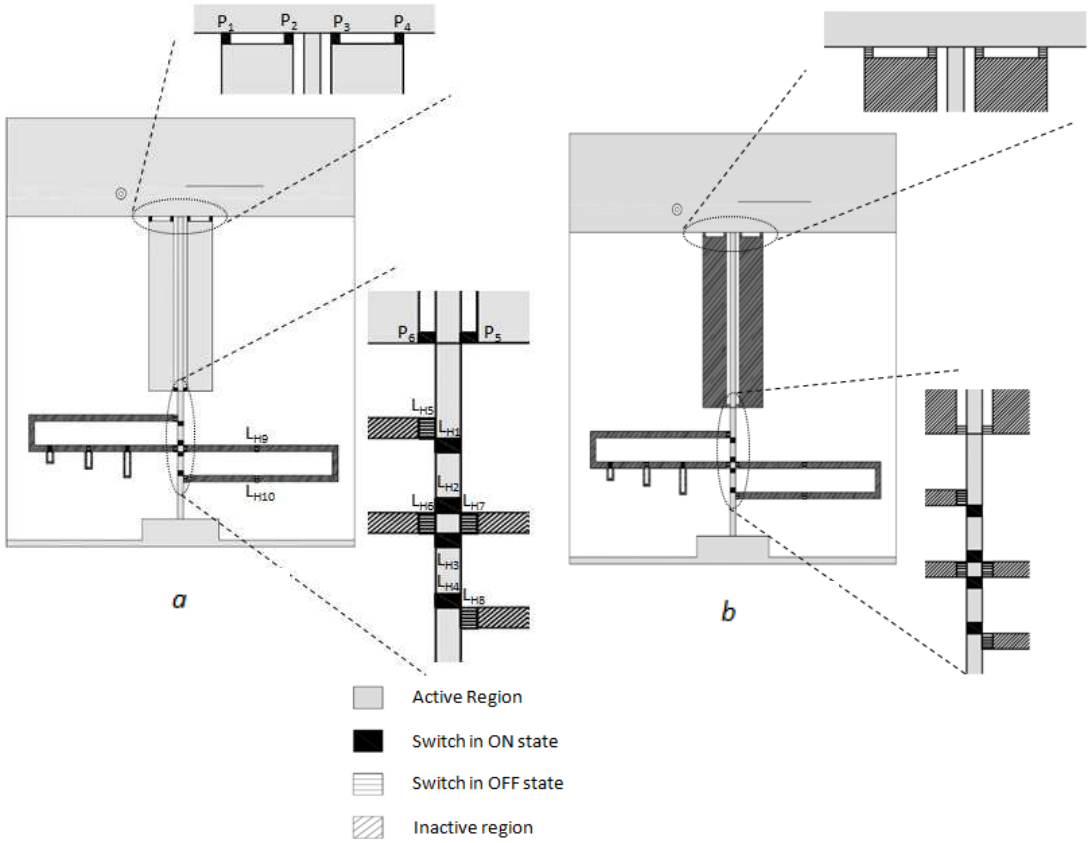

Fig. 3.5: Reconfigurable ground layer in Mode2: a) Configuration in sub-band 1 (406 – 452 MHz), b) Configuration in sub-band 2 (452 – 512 MHz).

same structure resonate at a higher frequency and also enhance the BW simultaneously. In an attempt to increase the bandwidth of the antenna in Mode2 (406 – 512 MHz) from approximately 50 MHz to 106 MHz (to cover the entire band which is 406 – 512 MHz) several parameters of the ground plane are varied the important one among them being pole-width which is represented as W_P in fig. 3.1. The parametric variation of the pole width (W_P) gave interesting results as shown in fig. 3.6. Ultimately, it became evident that a change in pole-width from 33mm to 3mm resulted in a jump in frequency adequate to cover the entire band of Mode2 (406 – 512 MHz) in two sub-bands. Hence, the reconfigurability in the pole structure is required to fine tune the Mode2 from 406 – 452 MHz band to 452 – 512 MHz band as the maximum BW obtained in this design is approximately 50 MHz. The switches P_1 to P_6 in the pole structure as shown in fig. 3.5 retune Mode2 to two sub-bands and

their operation is explained in Table 3.1. The switches L_{H5} to L_{H10} on the meandered line avoid the RF signal in taking a meandered way and force it to pass through the switches L_{H1} to L_{H4} in a straight line. The reflection coefficient in fig. 3.7 shows the two sub-bands of Mode2. The radiation pattern in fig. 3.8 at different frequencies in Mode2 shows an acceptable omni-pattern in $\phi = 0^0$ plane with a difference in the maximum and minimum gain of nearly 2 dB demonstrating the integrity in radiation pattern. The radiation pattern is not perfectly omni-directional as we have to compromise on the compactness of the

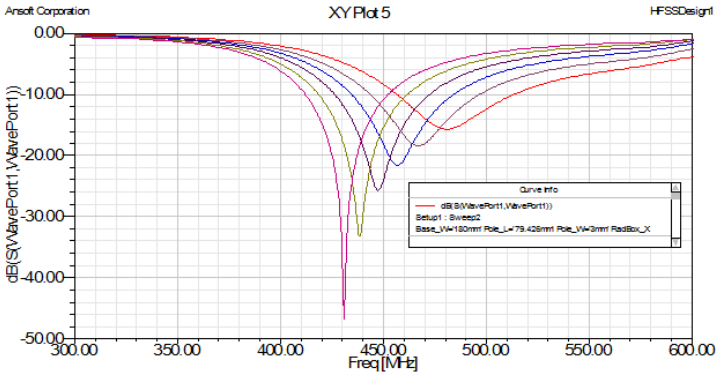

Fig. 3.6: Parametric variation of pole-width affecting the reflection coefficient of the antenna in Mode2.

Table 3.1: Switch operation for fine tuning in Mode2.

Frequency Range	Switches P_1 to P_6
406 – 452 MHz	ON
452 – 512 MHz	OFF

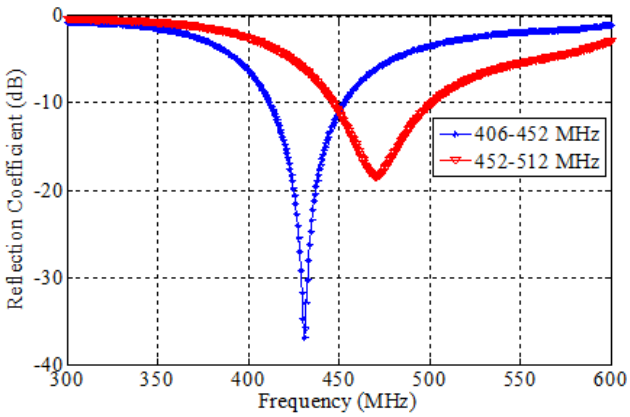

Fig. 3.7: Reflection coefficient in Mode2 depicting sub-bands 1 and 2.

antenna and BW required. Table 3.2 explains the operation of the switches in reconfiguring between Mode1 and Mode2.

3.3 Surface Current Distribution on the Reconfigurable Ground Layer in Different Modes of Operation

The surface current distribution on the reconfigurable ground layer is an important parameter to explain the resulting bandwidth, corresponding shape of the radiation pattern and operational frequency of the FRA. Figure 3.9 shows the surface current distribution on the reconfigurable ground layer in switching from Mode1 (152-162 MHz) to Mode2 (406-512 MHz) which is also called coarse tuning.

Also fig. 3.10 shows the High Frequency Structure Simulator (HFSS) plot of surface current distribution of fig. 3.9. As is evident from fig. 3.9, the surface current is made to flow in a meandered way to the T-shape in Mode1 to decrease the operational frequency

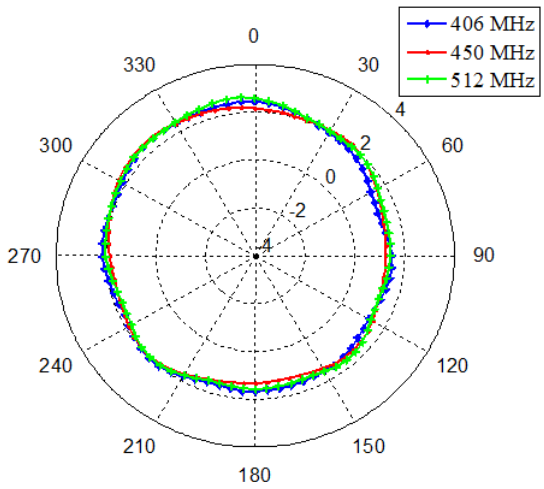

Fig. 3.8: Radiation pattern in the $\phi = 0^0$ plane in Mode2 at different frequencies.

Table 3.2: Switch operation in frequency switching from Mode1 to Mode2.

Mode of Operation	Mode1(152 – 162 MHz)	Mode2(406 – 512 MHz)
L_{H1} to L_{H4}	OFF	ON
L_{H5} to L_{H10}	ON	OFF
P_1 to P_6	ON	ON/OFF based on sub-band
L_1, L_4 *and* L_7	ON	OFF
L_2, L_3 , L_5 *and* L_6	ON/OFF based on fine tune	OFF

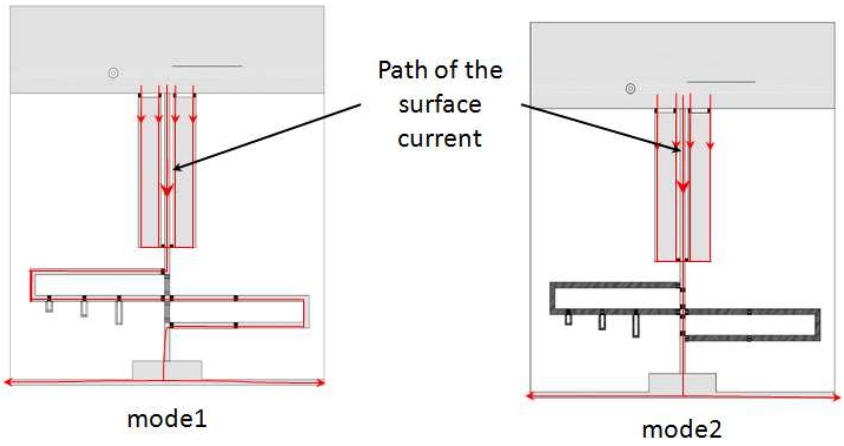

Fig. 3.9: Surface current distribution on Mode1 and Mode2 ground plane configurations.

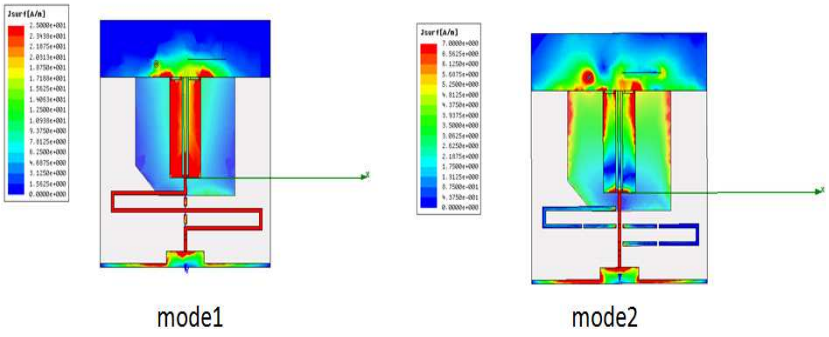

Fig. 3.10: Surface current distribution of Mode1 and Mode2 in HFSS.

(as the operational frequency is inversely proportional to the length of the path traversed by the surface current) as opposed to a straight line path to the T-shape in Mode2 for the same structure, hence accomplishing the goal of frequency reconfigurability with minimum number of switches in a single layer. The corresponding switch operation is given in Table 3.2. In Mode1, as the surface current traverses through many turns the bandwidth is reduced justifying the use of fine tuning for Mode1. In this FRA design, the pole in the ground-plane is the major radiating element due to the coupling effect over a small distance from the radiation patch, accordingly explaining the omni-directional radiation pattern in the $\phi = 0^0$ plane. The 3D radiation pattern of the antenna in Mode1 is shown in fig. 3.11 to effectively explain the radiating nature of the pole. Figure 3.12 shows the surface current distribution (in red lines) of some of the fine-tuned modes in Mode1 indirectly explaining the different combinations of opening and closing of switches L_1 to L_9. Finally, to switch

between the sub-bands in Mode2, figs. 3.13 and 3.14 explain the path traversed by the surface current, effectively creating a reconfigurable pole structure with the switch operation explained in Table 3.1.

3.4 Frequency Reconfigurability including the 700 - 900 MHz Band

Ultimately, the aim of this FRA is to cover all the PS bands (152-162 MHz, 400-500 MHz, 700-900 MHz, and 4.9 GHz). In an attempt to do so, the structure which is resonating in Mode2 is also checked if it resonates in the range 700-900 MHz by setting the frequency sweep in HFSS from 600 MHz to 1 GHz. The reason behind doing this is to cover the entire frequency range of interest with minimal changes in the reconfigurable ground plane of the antenna. The result of this investigation in terms of reflection coefficient is given in fig. 3.15 which surprisingly confirms the presence of resonance over a huge BW from 680 MHz to 920 MHz. Finally, after a series of HFSS simulations it was concluded that making small changes to the design parameters namely, shorting-wall width, position of the shorting wall from the corner of the radiation patch and width of the pole (W_P) Mode1 and Mode2 can cover 150, 400 - 500, and 700 - 900 MHz bands with minimal number of switches in the

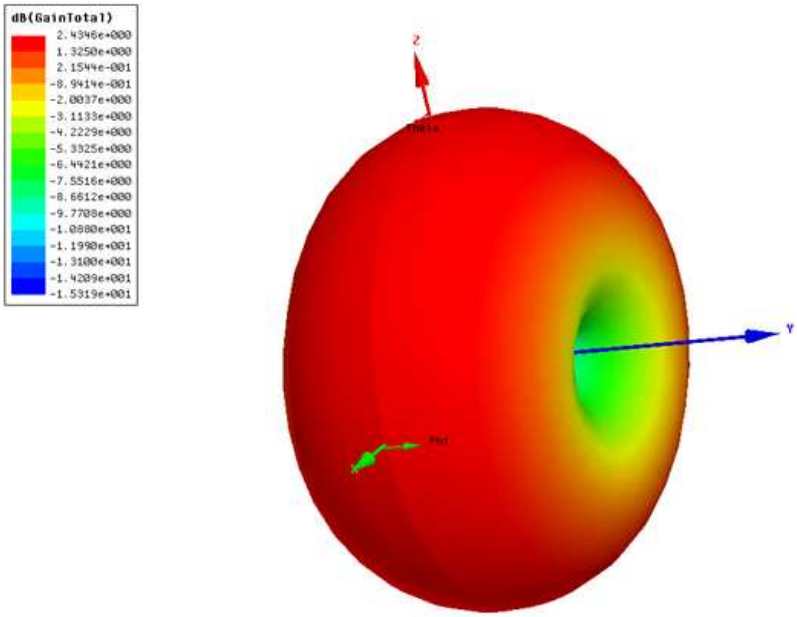

Fig. 3.11: 3D radiation pattern at 157 MHz.

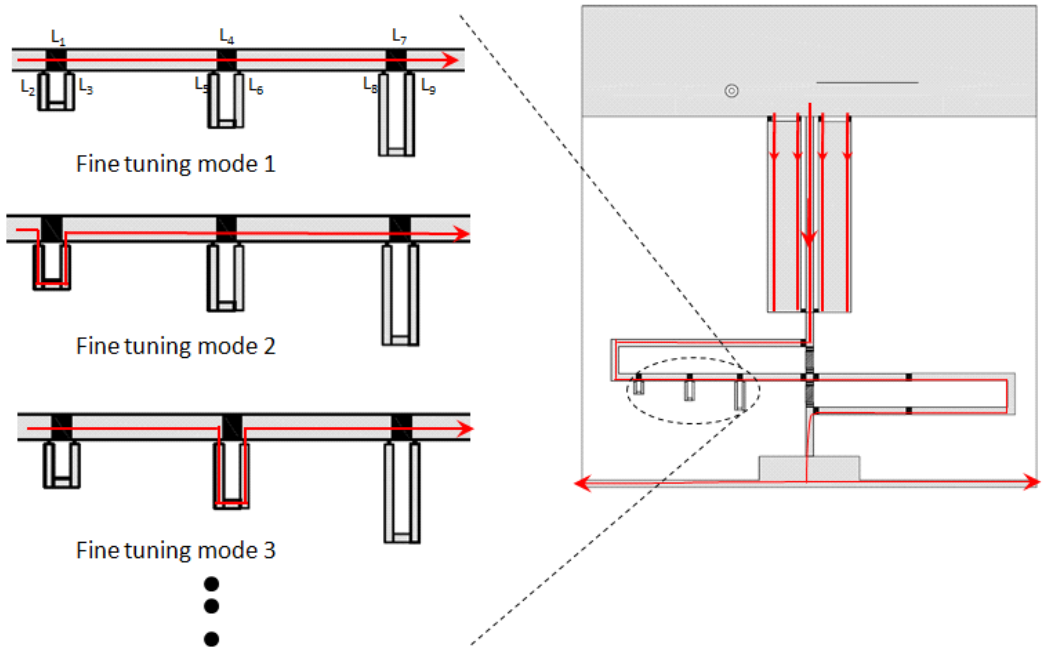

Fig. 3.12: Surface current distribution in fine tuning of Mode1.

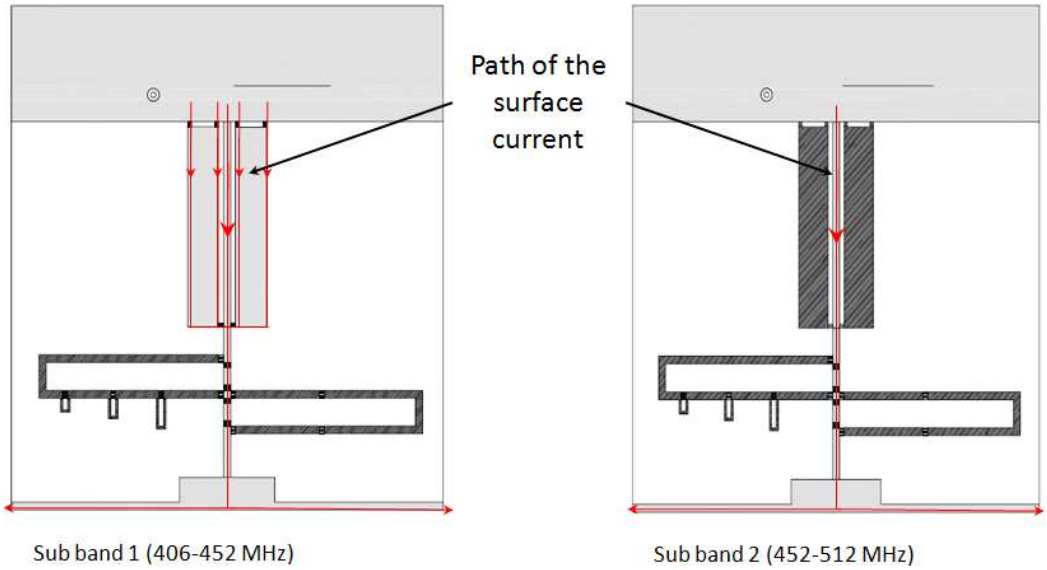

Fig. 3.13: Surface current distribution in fine tuning of Mode2.

ground plane. It is important to note that, the radiation pattern in 700 - 900 MHz range further degrades in terms of being omni-directional, the reason being the inevitable coupling effect from the radiation patch. Especially, the worst radiation pattern is seen at 700 and 750 MHz and the pattern seems to improve (in terms of being omni-directional) at higher

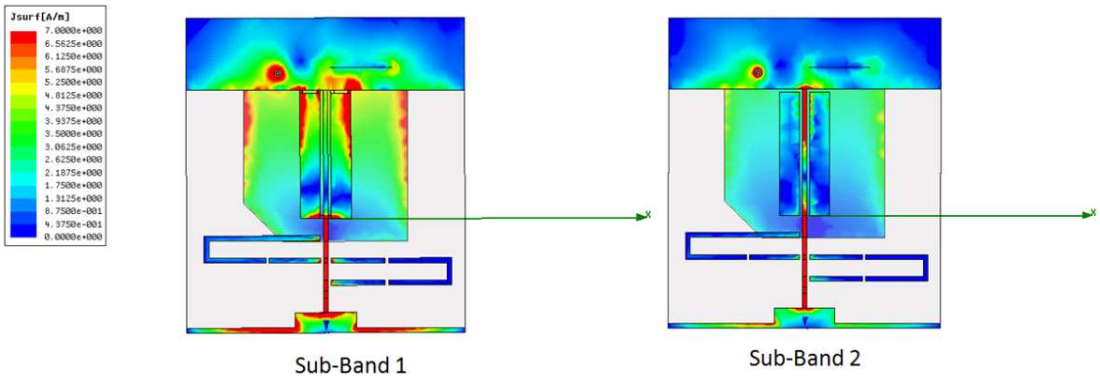

Fig. 3.14: Surface current distribution in HFSS depicting fine tuning of Mode2.

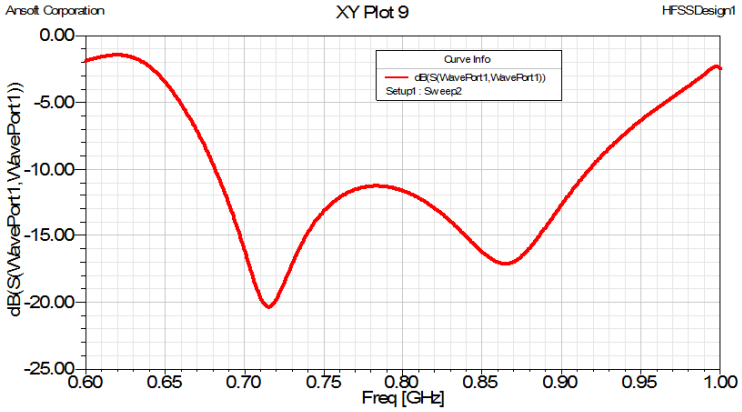

Fig. 3.15: Reflection coefficient of Mode2 (sub-band 1) representing first attempt to find resonance in the range in 600 MHz to 1 GHz range.

frequencies (800, 850, and 900 MHz) as shown in fig. 3.16. The final design results in terms of reflection coefficient and radiation pattern are given in figs. 3.17 and 3.18. Figure 3.17 shows that Mode2, sub-band 1 covers both 400-450 MHz and 700 - 900 MHz bands in a dual band configuration where as sub-band 2 of Mode2 covers only 450 - 500 MHz band. The final design dimensions in mm are given as, the patch, L_p X W_p is 107.47 X 105.96; the height of the patch, $h = 25$; the tapering lengths, $A = 93.9$, $B = 90.9$; the ground plane parameters L_t X W_g is 180 X 195, $W = 20$; $W_t = 6$; the width of the shorting wall is $W_s = 30$, pole-width W_P varied between 3 mm and 33.

3.5 Method of Fabrication

The overall size in *cm* of the reconfigurable antenna is 19.5 X 18 X 2.5 which is not

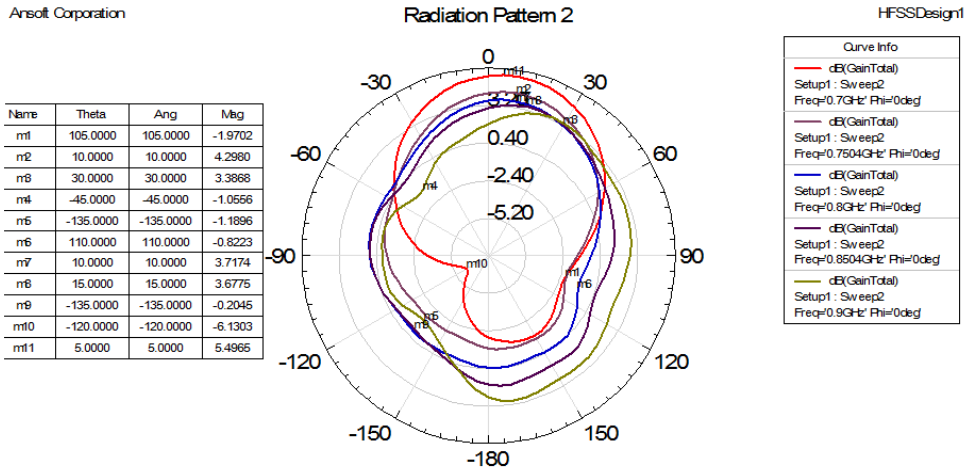

Fig. 3.16: Radiation pattern in 700 - 900 MHz range.

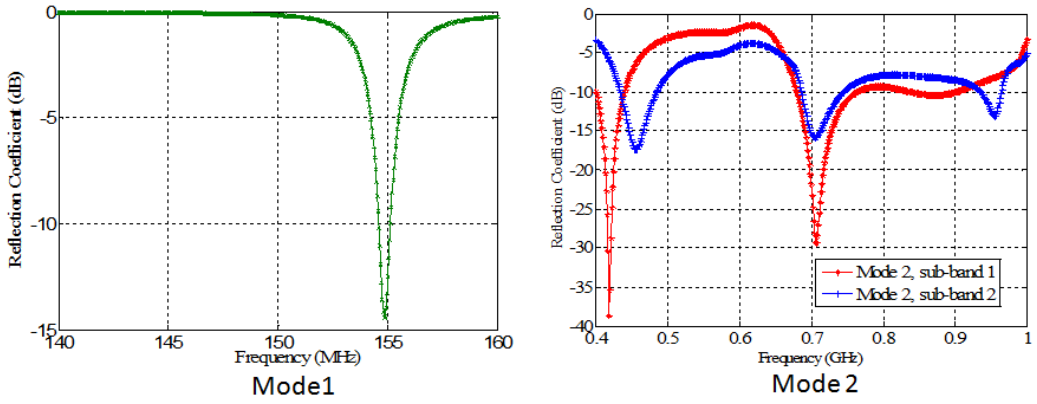

Fig. 3.17: Reflection coefficient in Mode1 and Mode2 including 700 - 900 MHz band.

micro-fabrication compatible. However, the advantage of this design is that the MEMS switches are concentrated at four regions in the reconfigurable ground layer. Hence, as shown in fig. 3.19, four different substrates with MEMS are fabricated seperately and finally integrated with the dummy antenna (fabricated using a milling machine). The final stucture of the reconfigurable after MEMS integration is shown in fig. 3.20.

The microfabrication process of MEMS switch [8] was performed based on the microwave laminate compatible RF MEMS technology [18, 19] that enables the monolithic integration of MEMS actuators with antenna segments.

A seven-step microfabrication process using microwave laminate TMM10i substrates is developed. The microfabrication process would begin by wet-etching and chemical mechan-

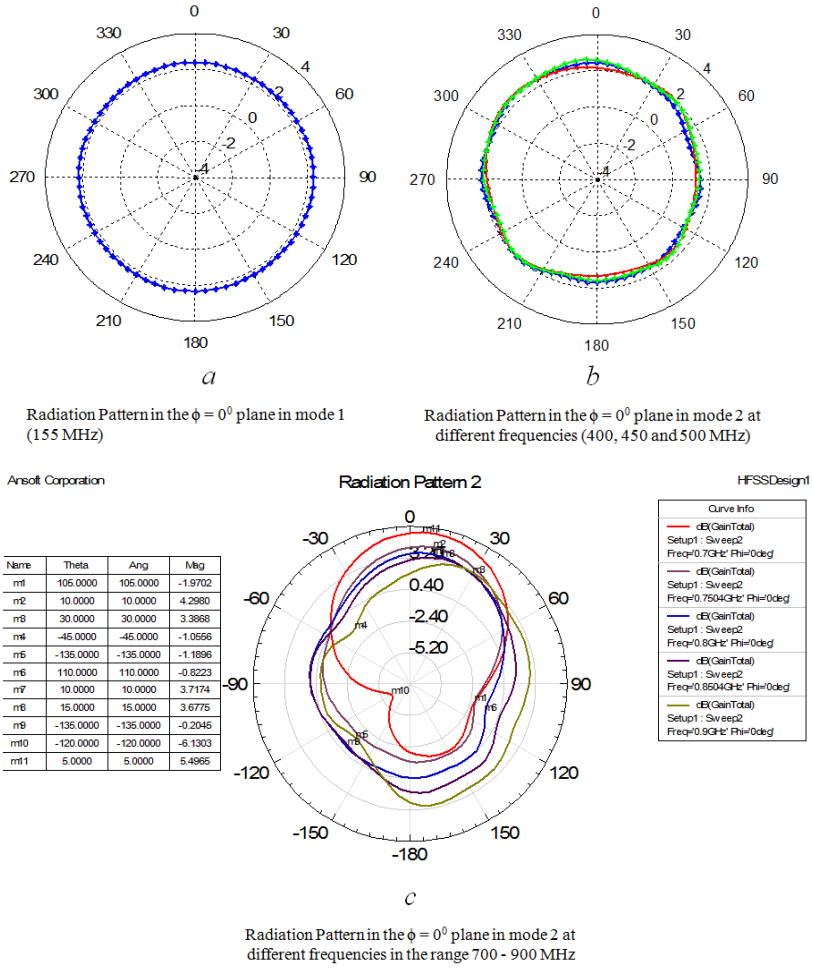

Fig. 3.18: Radiation pattern at all frequencies in Mode1 and Mode2.

ical polishing (CMP) the 15 μm-thick Cu layer on top of the microwave laminate TMM10i substrate down to $\sim 2\mu$m. Afterwards, the different regions of interest of the RA and microstrip line segments would be patterned and wet-etched selectively. Next, $\sim$ 200 nm thick SiCr bias lines were formed by DC-sputtering which was followed by the formation of Ti/Cu bias electrode pads. A $\sim 2\mu$m thick Ti/Cu island metal is deposited as the central-base metallic pad for the MEMS cantilever beam. In the fifth step, bias lines and bias electrodes are passivated with a 250 nm thick dielectric layer. This is followed by the deposition of a thick ($\sim 3\mu$m) amorphous Si (a:Si) sacrificial layer which would be planarized using CMP. In the final seventh step, a $\sim$ 1.0 μm thick TiW layer is sputtered. After dry-release process, the cantilevers (width = 350μm and length = 650μm) curled upwards due to the inter-

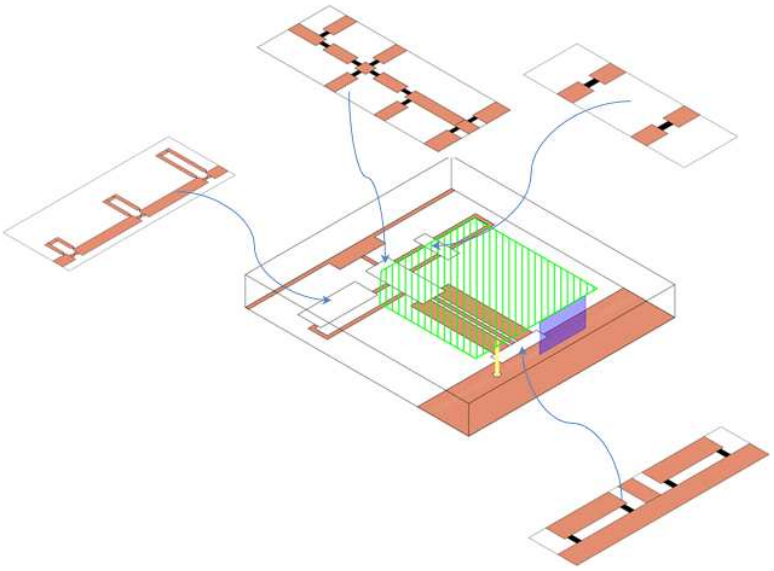

Fig. 3.19: MEMS integration with the overall design.

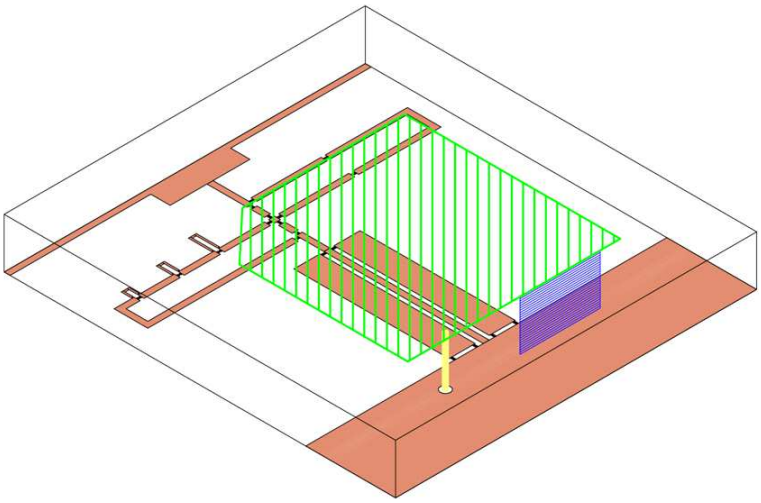

Fig. 3.20: Overall structure of the reconfigurable antenna.

nal stress-gradient within the deposited TiW. Figure 3.21 summarizes the microfabrication process steps used for double-arm MEMS actuators.

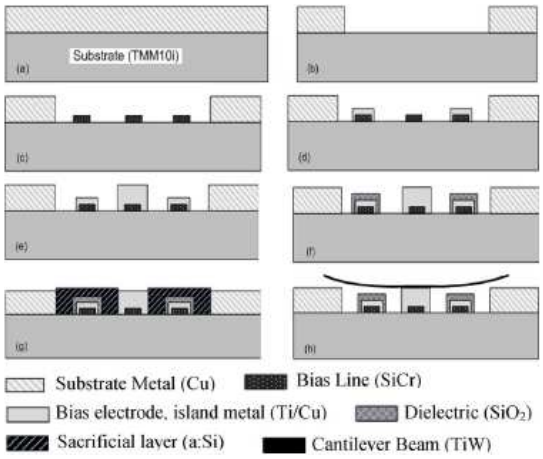

Fig. 3.21: Microfabrication process steps for the double-arm MEMS actuator.

Chapter 4

Robust Mechanical Design of MEMS Switch

4.1 Introduction

For the successful design of a reconfigurable antenna, reliable operation of its building blocks - MEMS switches, over billions of life-cycles is quite essential. The switch employed to reconfigure the frequency is a DC-Contact RF MEMS switch [14] with superior RF performance in terms of insertion loss and isolation. Instead of using the double arm MEMS switch described in the previous chapter, a single arm DC-Contact RF MEMS Series switch [14] is used which is similar to the Radant MEMS switch [36] as a first step in developing reliable MEMS switch. This chapter mainly deals with the mechanical design of the MEMS switch by an Electro Mechanical Software CoventorWare in which the analysis is broadly divided into four categories - Pull-in-Analysis, Stress-Analysis, Trajectory Analysis, and Dynamic Analysis.

Before going to the different analyses, the 3D modeling of MEMS switch is performed by describing its fabrication procedure and the corresponding layout in coventor. There is also Material Properties Database (MPD) in coventor to assign different materials according to the problem specified. The mechanical design can be done in two ways in coventor using Analyzer (which employs Finite Element Method (FEM) for the solution) or using Architect (which solves the differential equations in closed form). In Analyzer, the process flow and the layout information are utilized to get a 3D model (scaled by a factor of 10 in the z-direction for better detail) as shown in fig. 4.1, which is close to the real-life MEMS switch. On the other hand, the Architect uses interconnected parametric components to form a system level MEMS switch as shown in fig. 4.2. The 3D figure obtained from Architect looks similar to the 3D figure from Analyzer; however, Architect simulations are much faster than Analyzer as the latter employs FEM to solve the problem. Pull-in, Trajectory,

and Stress Analyses are better performed by Analyzer and for Dynamic Analysis Architect is the best option as it is time-consuming and memory intensive to use Analyzer in this regard.

4.2 Pull-in and Trajectory Analysis

The voltage (applied to the actuation pad) at which the mechanical restoring force of the cantilever is overcome by the electrostatic force between the actuation pad and cantilever as a result of which the cantilever comes into contact with the contact pad is the Pull-down or Pull-in Voltage of a DC Contact MEMS Switch and is given as $V_{pull-down} = \sqrt{\frac{8k}{27\epsilon_0 W w}{g_0}^3}$ [14] where W is the length of the actuation pad, w is the width of cantilever,

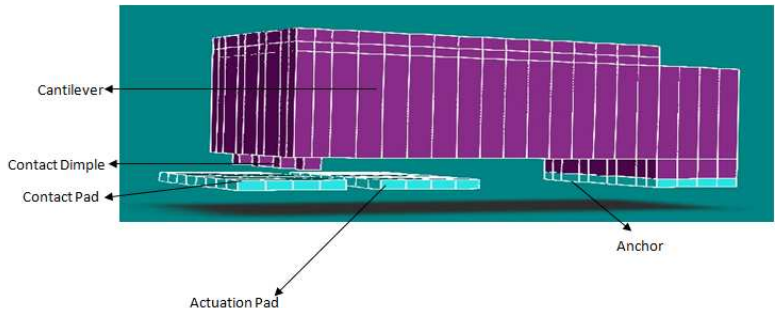

Fig. 4.1: 3D meshed model in coventor ready for FEM.

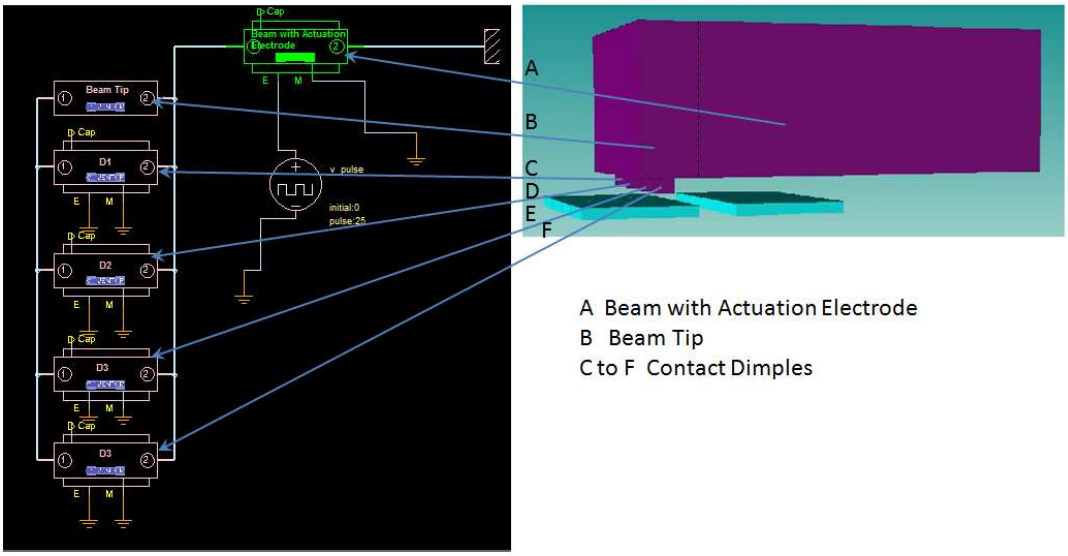

Fig. 4.2: Architect model with the corresponding 3D schematic.

k is the spring constant of the cantilever beam which in turn depends on Young's modulus (E) as explained in Appendix C, $g_0 = h - 0.3\mu m$ is the height of the cantilever above the actuation pad, and ϵ_0 is the permittivity of free space. The different parts of the DC Contact RF MEMS switch are clearly depicted in fig. 4.3. To have a good contact in order to minimize the contact resistance [37] (which in turn decreases the insertion loss), the actuation voltage should be 1.5 times the Pull-down voltage. However, generally the actuation voltage of a MEMS switch should not be too high. To get the best out of this trade-off the dependence of Pull-down Voltage on cantilever thickness (t) is subject to a variation to obtain the optimum actuation voltage for the MEMS switch. The voltage at which the cantilever becomes unstable and collapses on the actuation pad (which we will call collapse voltage for simplicity) is important because this should be avoided to prevent shorting of RF energy to actuation pad and this phenomenon is best shown in fig. 4.4. The other parameters, like length of the cantilever beam (l), width of cantilever (w which is not shown in fig. 4.3), height of cantilever above the substrate (h), dimple thickness (d), are kept constant during the process. Table 4.1 gives the Pull-down and collapse voltages for different thicknesses of cantilever.

4.3 Stress Analysis

From the results of the previous section, the cantilevers with 4 μm and 5 μm thicknesses are selected for stress analysis as these two cases suit best to design a robust MEMS switch from the previous analysis. During the dry-release process of sacrificial layer to form the

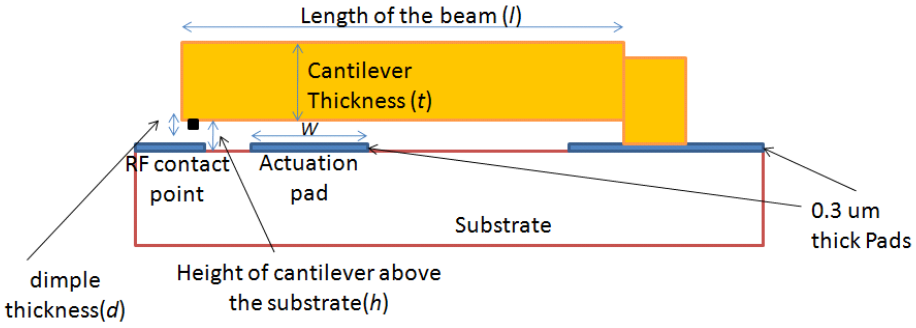

Fig. 4.3: DC contact MEMS switch with different parts clearly depicted.

MEMS cantilever [15], a residual stress in the cantilever is inevitable as a result of which the cantilever is curled a little up or down basing on the type of stress gradient. This effect is detrimental to the acceptable RF performance of the MEMS switch (described in the previous chapter) as it can reduce the isolation or increase the insertion loss depending on the type of stress gradient [14]. Table 4.2 shows the CoventorWare results of stress analysis of 4 μm and 5 μm cantilever beams where the displacement of the tip of the cantilever beam for a particular stress value is shown. In Table 4.2, a negative value for displacement indicates that the cantilever beam bends towards the RF contact point and vice versa.

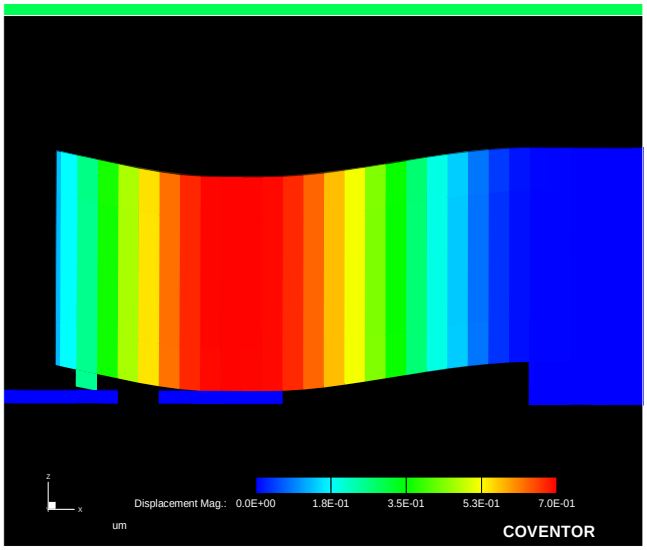

Fig. 4.4: Collapse of cantilever beam on actuation pad.

Table 4.1: Pull-down and collapse voltages for different cantilever thicknesses.

Cantilever thickness($t\mu m$)	Pull-down Voltage(V)	Collapse Voltage(V)
2	10.2	27.7
3	18.2	50.4
4	28.5	78
5	39	106
6	50.3	141
7	62.5	190
8	76	220

4.4 Dynamic Analysis

After initial analysis, fabrication and testing of MEMS switch it was found that before the cantilever creates a good contact with the RF contact point the beam touches the actuation pad creating a DC short. Hence, to better visualize this effect, dynamic analysis of the beam is carried out in Architect where a fixed voltage can be applied to the beam and over time the motion of the beam can be visualized in a video. In this analysis it was found that the effect of dimple thickness (d), height of the cantilever above the substrate(h), and thickness of the cantilever (t) have a predominant effect on DC shorting which can be seen in fig. 4.4. Accordingly, the thickness of the cantilever is chosen to be 4 μm or 6 μm and h is chosen to be 0.7 μm or 1.05 μm, giving four combinations, and for each case dimple thickness (d) is varied from 0.1 μm to 0.6 μm. Tables 4.3, 4.4, 4.5, and 4.6 give the status of the cantilever beam for a particular dimple thickness when actuation voltage is two times the Pull-down voltage for all four cases. Also, the Young's modulus of the cantilever beam practically obtained is never greater than 35 GPa [38]. Hence, to be more realistic the Young's modulus of the simulated beam is delibrately reduced to 28.5 GPa and under these circumstances the results are given as follows.

Table 4.2: Stress analysis.

Residual Stress	Displacement for 4 μm beam	Displacement for 5 μm beam
$-100MPa$	-0.15μm	-0.13μm
$-50MPa$	-0.093μm	-0.075μm
$50MPa$	0.037μm	0.045μm
$100MPa$	0.094μm	0.1μm

Table 4.3: Status of the beam (t=6 μm, h=1.05 μm, $V_{actuation} = 140V$).

Dimple thickness(d in μm)	Status
0.1	collapses
0.2	collapses
0.3	collapses
0.4	collapses
0.5	works
0.6	works

Table 4.4: Status of the beam (t=6 μm, h=0.7 μm, $V_{actuation} = 75V$).

Dimple thickness(d in μm)	status
0.1	collapses
0.2	collapses
0.3	works
0.4	works
0.5	works
0.6	works

Table 4.5: Status of the beam (t=4 μm, h=1.05 μm, $V_{actuation} = 75V$).

Dimple thickness(d in μm)	status
0.1	collapses
0.2	collapses
0.3	collapses
0.4	collapses
0.5	collapses
0.6	works

Table 4.6: Status of the beam (t=4 μm, h=0.7 μm, $V_{actuation} = 40V$).

Dimple thickness(d in μm)	status
0.1	collapses
0.2	collapses
0.3	works
0.4	works
0.5	works
0.6	works

Chapter 5

Conclusion and Future Work

Finally, with the robust mechanical design of the MEMS switch, which is the fundamental building block of the reconfigurable antenna supported by a compact and broadband antenna structure, a harsh-environment tolerant frequency reconfigurable antenna can be made, which becomes extremely useful to the Public Safety personnel in handling catastrophic situations. Improvements in microfabrication process steps to aid in the reliability of MEMS switch accompanied by the fabrication of overall design of the frequency reconfigurable antenna is the future work to the thesis presented here, which I would be carrying out as a doctoral effort.

References

[1] D. Gesbert, M. Shafi, D.-S. Shiu, P. J. Smith, and A. Naguib, "From theory to practice: an overview of mimo space-time coded wireless systems," *Selected Areas in Communications, IEEE Journal*, vol. 21, no. 3, pp. 281–302, Apr. 2003.

[2] S. A. Jafar and S. Shamai, "Degrees of freedom region for the mimo x channel," *Computing Research Repository*, vol. abs/cs/0607099, 2006.

[3] L. Amos, S. Shlomo, and A. W. Michele, "On the capacity of fading mimo broadcast channels with imperfect transmitter side-information," *Computing Research Repository*, vol. abs/cs/0605079, 2006.

[4] M. Maddah-Ali, A. Motahari, and A. Khandani, "Signaling over mimo multi-base systems: Combination of multi-access and broadcast schemes," in *Information Theory, 2006 IEEE International Symposium*, pp. 2104–2108, July 2006.

[5] H. Weingarten, "On the compound mimo broadcast channel," in *Proceedings of Annual Information Theory and Applications Workshop University of California, San Diego*, 2007.

[6] B. A. Cetiner, Chapter 9 in *MIMO Antenna Technology for Wireless Communications, Electrical Engineering and Applied Signal Processing Series.* Boca Raton, FL: CRC Press, 2006.

[7] B. A. Cetiner and H. Jafarkhani, "Method and apparatus for an adaptive multiple-input multiple-output $MIMO$ wireless communications systems," Patent US 7,469,152 B2, Dec. 2008.

[8] B. A. Cetiner, G. R. Crusats, L. Jofre, and N. Biyikli, "Rf mems integrated frequency reconfigurable annular slot antenna," *Antennas and Propagation, IEEE Transactions*, vol. 58, no. 3, pp. 626–632, Mar. 2010.

[9] B. A. Cetiner, H. Jafarkhani, J.-Y. Qian, H. J. Yoo, A. Grau, and F. De Flaviis, "Multifunctional reconfigurable mems integrated antennas for adaptive mimo systems," *Communications Magazine, IEEE*, vol. 42, no. 12, pp. 62–70, Dec. 2004.

[10] B. A. Cetiner, J. Y. Qian, G. P. Li, and F. De Flaviis, "A reconfigurable spiral antenna for adaptive mimo systems," *European Association for Signal Processing, International Journal of Wireless Communications and Networking*, no. 3, pp. 382–389, 2005.

[11] L. N. Pringle, P. H. Harms, S. P. Blalock, G. N. Kiesel, E. J. Kuster, P. G. Friederich, R. J. Prado, J. M. Morris, and G. S. Smith, "A reconfigurable aperture antenna based on switched links between electrically small metallic patches," *Antennas and Propagation, IEEE Transactions*, vol. 52, no. 6, pp. 1434–1445, June 2004.

[12] B. A. Cetiner and N. Biyikli, "Penta-band planar inverted f-antenna (pifa) integrated by rf-nems switches," in *University/Government/Industry Micro/Nano Symposium, 2008. UGIM 2008. 17th Biennial*, pp. 116–119, July 2008.

[13] B. Yildirim, B. A. Cetiner, and Q. Xu, "Reconfigurable planar inverted f antenna for mobile phones," *presented at the 2007 IEEE International Symposium on Antennas & Propagation*, pp. 5207–5210, 2007.

[14] G. M. Rebeiz, *RF MEMS Theory, Design and Technology.* Hoboken, NJ: John Wiley & Sons, 2003.

[15] N. Biyikli, Y. Damgaci, and B. A. Cetiner, "Low-voltage small-size double-arm mems actuator," *Electronics Letters*, vol. 45, no. 7, pp. 354–356, 2009.

[16] H.-P. Chang, J. Qian, B. Cetiner, F. De Flaviis, M. Bachman, and G. Li, "Design and process considerations for fabricating rf mems switches on printed circuit boards," *Journal of Microelectromechanical Systems*, vol. 14, no. 6, pp. 1311–1322, Dec. 2005.

[17] B. A. Cetiner, B. S. Yildirim, N. Biyikli, and Y. Damgaci, "Nanoelectromechanical switches for reconfigurable antenna applications," *accepted for publication in the Microwave and Optical Technology Letters*, 2009.

[18] B. A. Cetiner, J. Y. Qian, H. P. Chang, M. Bachman, G. P. Li, and F. De Flaviis, "Monolithic integration of rf mems switches with a diversity antenna on pcb substrate," *Microwave Theory and Techniques, IEEE Transactions*, vol. 51, no. 1, pp. 332–335, Jan. 2003.

[19] B. A. Cetiner, M. Bachman, G.-P. Li, J. Qian, H.-p. Chang, and F. De Flaviis, "Mems fabrication on a laminated substrate," Patent 20 050 062 653, Mar. 2005 [Online]. Available: `http://www.freepatentsonline.com/y2005/0062653.html`.

[20] C. P. Sukumar, H. Eslami, A. M. Eltawil, and B. A. Cetiner, "Link performance improvement using reconfigurable multiantenna systems," *Antennas and Wireless Propagation Letters, IEEE*, vol. 8, pp. 873–876, 2009.

[21] V. R. Cadambe and S. A. Jafar, "Interference alignment and degrees of freedom of the -user interference channel," *Information Theory, IEEE Transactions*, vol. 54, no. 8, pp. 3425–3441, Aug. 2008.

[22] V. R. Cadambe and S. A. Jafar, "Interference alignment and the degrees of freedom of wireless networks," *Information Theory, IEEE Transactions*, vol. 55, no. 9, pp. 3893–3908, Sept. 2009.

[23] V. R. Cadambe, S. A. Jafar, and S. Shamai, "Interference alignment on the deterministic channel and application to fully connected gaussian interference networks," *Information Theory, IEEE Transactions*, vol. 55, no. 1, pp. 269–274, Jan. 2009.

[24] V. R. Cadambe, S. A. Jafar, and C. Wang, "Interference alignment with asymmetric complex signaling - settling the host-madsen-nosratinia conjecture," *Computing Research Repository*, vol. abs/0904-0274, 2009.

[25] M. A. Maddah-Ali, A. S. Motahari, and A. K. Khandani, "Communication over mimo x channels: Interference alignment, decomposition, and performance analysis," *Information Theory, IEEE Transactions*, vol. 54, no. 8, pp. 3457–3470, Aug. 2008.

[26] B. Nazer, M. Gastpar, S. A. Jafar, and S. Vishwanath, "Ergodic interference alignment," in *Proceedings of the International Symposium on Information Theory (ISIT 2009), Seoul, South Korea*, pp. 1769–1773, 2009.

[27] U. Niesen, "Interference alignment in dense wireless networks," *Computing Research Repository*, vol. abs/0912.0868, 2009.

[28] C. Suh and D. Tse, "Interference alignment for cellular networks," in *Communication, Control, and Computing, 2008 46th Annual Allerton Conference*, pp. 1037–1044, Sept. 2008.

[29] K. Hirasawa and M. Haneishi, *Analysis, Design, and Measurement of Small Low Profile Antennas*. Norwood, MA: Artech House, 1992.

[30] J. D. Krauss and R. J. Marhefka, *Antennas For All Applications*. New York: McGraw Hill, 2002.

[31] F. Wang, Z. Du, Q. Wang, and K. Gong, "Enhanced-bandwidth pifa with t-shaped ground plane," *Electronics Letters*, vol. 40, no. 23, pp. 1504–1505, Nov. 2004.

[32] C. K. Byung, D. P. Ju, and D. C. Hyung, "Tapered type pifa design for mobile phones at 1800 mhz," in *Vehicular Technology Conference, 2003. VTC 2003-Spring. The 57th IEEE Semiannual*, vol. 2, pp. 1012–1014, Apr. 2003.

[33] A. F. Muscat and C. G. Parini, "Novel compact handset antenna," *IEE Conference Publications*, no. CP480, pp. 336–339, 2001 [Online]. Available: `http://link.aip.org/link/abstract/IEECPS/v2001/iCP480/p336/s1`.

[34] G. A. E. Vandenbosch, "Capacitive matching of microstrip antennas," *Electronics Letters*, vol. 31, no. 18, pp. 1535–1536, Aug. 1995.

[35] A. Khoshniat, H. S. Mopidevi, and B. A. Cetiner, "Broadband capacitively fed tapered type pifa with modified ground plane," *Electronics Letters*, vol. 46, no. 7, pp. 474–475, Jan. 2010.

[36] S. Majumder, J. Lampen, R. Morrison, and J. Maciel, "A packaged, high-lifetime ohmic mems rf switch," in *Microwave Symposium Digest, 2003 IEEE MTT-S International*, vol. 3, pp. 1935–1938, June 2003.

[37] S. Timsit, "Electrical contact resistance: properties of stationary interfaces," in *Electrical Contacts, 1998., Proceedings of the Forty-fourth IEEE Holm Conference*, pp. 1–19, Oct. 1998.

[38] S. Kal, A. Bagolini, B. Margesin, and M. Zen, "Stress and resistivity analysis of electrodeposited gold films for mems application," *Microelectronics Journal*, vol. 37, no. 11, pp. 1329–1334, 2006.

Appendices

Appendix A

Overall Research Flow at RF μNϵMS Lab.

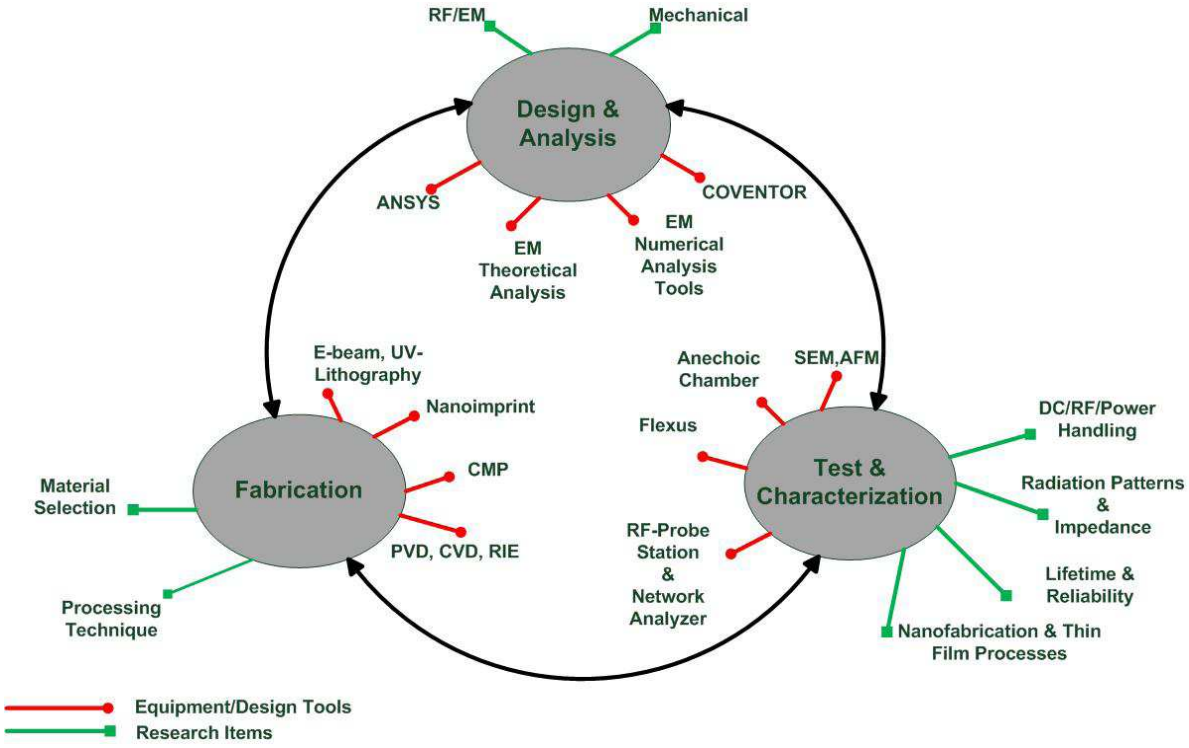

Fig. A.1: Overall research flow at RF μNϵMS lab.

Appendix B

Antenna Basics

B.1 Radiation Pattern

In the field of antenna design the term "radiation pattern" most commonly refers to the directional (angular) dependence of radiation from the antenna. The radiation pattern is a graphical depiction of the relative field strength transmitted from or received by the antenna. Antenna radiation patterns are taken at one frequency, one polarization, and one plane cut. The patterns are usually presented in polar or rectilinear form with a dB strength scale. The antenna in this thesis is aimed to give an omni-directional radiation pattern in the $\phi = 0^0$ plane as it best suits the wireless communication requirements.

B.2 Directivity and Gain

The directivity D and the gain G defined in [28] are probably the most important parameters of an antenna. The directivity of an antenna is equal to the ratio of the maximum power density $P(\theta, \phi)_{max}(watts/m^2)$ to its average value over a sphere as observed in the far field of an antenna. Thus,

$$D = \frac{P(\theta, \phi)_{max}}{P(\theta, \phi)_{avg}} \quad Directivity\ from\ pattern.$$

The *gain* G of an antenna is an actual or realized quantity which is less than the directivity D due to ohmic losses in the antenna or its radome (if it is enclosed).

B.3 Reflection Coefficient and Bandwidth

The ratio of reflected power from the antenna to the input power is the reflection coefficient. The lower is the reflection coefficient value the lower is the reflected power and more power is input to the antenna.

The range of frequencies in which the reflection coefficient is within the acceptable value so that maximum power is input into the antenna is the bandwidth of the antenna. The fractional bandwidth is defined as

$FBW = \frac{f_2 - f_1}{f_c}$,

where f_2 is the upper frequency beyond which the reflection coefficient degrades, similarly f_1 is the lower frequency, and f_c is the frequency of operation of the antenna.

Appendix C

MEMS Basics

Cantilever beams are useful in many situations where it is inconvenient to fix both ends of the beam [13]. An example is the in-line series switch where the input t-line becomes a cantilever beam whose free end hangs over the output t-line (fig. C.1).

The spring constant due to a uniform force applied over the entire beam is given by

$$k_a = \frac{2Ew}{3}(\frac{t}{l})^3,$$

where E is the Young's modulus of the cantilever beam, w, t, and l is the width, thickness, and length of the cantilever, respectively, whereas the spring constant for a force distributed from x to l on the beam, as shown in fig. C.1, is given by:

$$k_c = \frac{2Ew}{3}(\frac{t}{l})^3 \frac{1-(x/l)}{3-4(x/l)^3+(x/l)^4}.$$

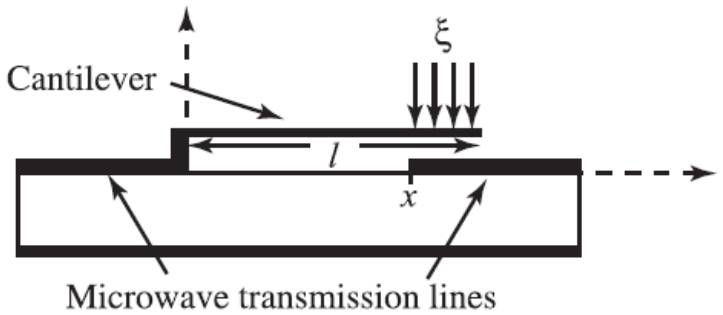

Fig. C.1: Example of a cantilever beam used as a series switch in a microstrip line.